Int. J. Environ. Sci. Technol. (2016) 13:907–926
DOI 10.1007/s13762-015-0928-5

ORIGINAL PAPER

# Role of bentonite adsorbent sub-layer in the photocatalytic-adsorptive removal of methylene blue by the immobilized $TiO_2$/bentonite system

**Y. S. Ngoh**[1] · **M. A. Nawi**[1]

Received: 14 July 2015 / Revised: 4 November 2015 / Accepted: 14 December 2015 / Published online: 7 January 2016


**Abstract** An immobilized clay composite (BEN–PVAG) on a glass plate (GP) was fabricated using bentonite powder (BEN) and glutaraldehyde cross-linked polyvinyl alcohol (PVAG) as the adsorbent and adhesive, respectively. The immobilized bentonite composite (BEN–PVAG) was characterized using SEM, EDX, FTIR, and BET analysis. The adsorption capacity of BEN–PVAG was examined using methylene blue (MB) as the model pollutant. The results indicated that the adsorption of MB onto BEN–PVAG obeyed pseudo-second-order kinetics. In addition, the adsorption of MB by the immobilized BEN–PVAG was controlled by intra-particle diffusion. In contrast, the adsorption of MB by the suspended BEN–PVAG composite was dominated by film diffusion. The immobilized BEN–PVAG was then applied as the adsorbent sub-layer for the fabrication of P-25$TiO_2$/BEN–PVAG/GP bilayer system where P-25$TiO_2$ was deposited as the top layer. The fabricated bilayer system exhibited synergistic photocatalytic-adsorptive removal of MB upon irradiation with a light source, while experiment in the dark yielded only adsorption process. The rate of the synergistic photocatalytic-adsorptive removal of MB by the P-25$TiO_2$/BEN–PVAG/GP was 5.3 times faster than the suspended P-25$TiO_2$. The result implied the positive impact of the BEN–PVAG adsorbent sub-layer on the immobilized P-25$TiO_2$ photocatalyst. Most important, the immobilized P-25$TiO_2$/BEN–PVAG/GP provided a convenient reuse of the catalyst over time where the treated water could be directly discharged without the need of filtration.

**Keywords** Kinetics · Bentonite · Immobilization · Methylene blue · $TiO_2$

## Introduction

The generation of effluents containing dyes by many industries is a major issue due to their adverse impact upon the environment and human beings. Dyes have high chemical and biological stability which requires effective remediation methods. Removal techniques of dye molecules from waste water include physical (Eren 2009; Gupta et al. 2013; Silva et al. 2012), chemical (Nawi and Sabar 2012; Saravanan et al. 2013) and biological processes (López et al. 2006; Selvakumar et al. 2010). Among these methods, adsorption using porous materials (Gupta and Saleh 2013) and heterogeneous photocatalysis (Gnanasekaran et al. 2015) had been demonstrated as promising techniques.

Photocatalysis process mainly involves the formation of highly oxidizing hydroxyl radicals, (HO·, $E^\circ = 2.8$ eV), that can attack the organic molecules and convert them entirely into $CO_2$ and $H_2O$ (Faisal et al. 2007). Nano-sized $TiO_2$ is widely applied as a photocatalyst because it is highly effective, non-toxic, of low cost and abundant (Rossetto et al. 2010). The photocatalytic process on the other hand is a surface-oriented process in which pre-adsorption of targeted pollutants within the vicinity of $TiO_2$ nanoparticles is necessary to allow effective oxidation of the substrates to occur. This is because the primary oxidizing radicals produced during photocatalysis are surface

**Electronic supplementary material** The online version of this article (doi:10.1007/s13762-015-0928-5) contains supplementary material, which is available to authorized users.

✉ M. A. Nawi
masri@usm.my

[1] School of Chemical Sciences, Universiti Sains Malaysia, 11800 Minden, Penang, Malaysia

bound hydroxyl radicals, which have extremely short lifespan of $10^{-9}$ s, and such phenomenon limits the radicals from diffusing to a long distance in the bulk solutions. Thus, only substrates which adhered to the photocatalyst surface can effectively react with the hydroxyl radicals (Radeka et al. 2014). However, $TiO_2$ suffers from low adsorption capacity and limited specific surface area. One way to overcome this shortcoming is to combine $TiO_2$ with adsorbents. In fact, many studies have shown that combining adsorbents with photocatalysts exhibited synergistic effects that enhanced the removal of the pollutants from the waste waters (Jamil et al. 2012; Rossetto et al. 2010).

Clays are one of the most investigated adsorbents for the removal of dyes due to their large specific surface area, large pore structure, high swelling capacity, high cations exchange capacity and inert chemical nature (Akar and Uysal 2010; Silva et al. 2012). Bentonite is a 2:1 type of clay in which its basic unit structure consists of two tetrahedral silica sheets and an octahedral aluminium hydroxide sheet. To date, bentonite has been investigated for the removal of not only dyes (Silva et al. 2012; Weng and Pan 2007) but also metal ions (Ararem et al. 2011) and polymers (Wang et al. 2013). Since bentonite has excellent adsorption ability, the integration of clays as supports for $TiO_2$-based photocatalysts are attracting increased attention, especially for enhanced elimination of dye molecules in textile wastewaters (Chen et al. 2013; Damardji et al. 2009; Hajjaji et al. 2013). The dispersion of $TiO_2$ nanoparticles onto clays not only improves its photocatalytic performance due to better adsorption of organic substrates, but also hinders the production of large catalyst aggregates that may decrease its catalytic efficiency (Chen et al. 2013).

Works on combining clays with photocatalysts were mostly carried out via pillaring method which utilized titanium precursors and followed by the calcination process (Damardji et al. 2009; Rossetto et al. 2010; Chen et al. 2013). Nevertheless, the $TiO_2$ crystallites that formed from these precursors within the interlayer of the clay may be too small in size, i.e. 2–3 nm for producing a good photocatalytic performance in the degradation of organic pollutants (Bovey et al. 2006; Zhu and Othman 2002). Moreover, although these $TiO_2$ pillared clays allowed more convenient recovery after water treatment due to their larger aggregates, filtration process was still required as the post-treatment step.

To overcome these drawbacks, there is a need to develop a new method for combining photocatalyst with clay, such as immobilization of $TiO_2$ nanoparticles onto the external surface of the clay composite in a layered manner on a rigid support instead of intercalating them into the interlayer of the clays. This can be regulated by preparing the photocatalyst and clay composite individually with the assistance of adhesive polymers and then assemble them in a layer by layer arrangement on glass supports. This deposition method allows the $TiO_2$ top layer to be constantly exposed under light irradiation, and thus, good photocatalytic performance can be expected. Each of the layers can also be modified and controlled independently to acquire the desired degree of photocatalysis and adsorption processes. Apart from that, the bilayer system also enables the designation of flow-through reactor for the removal of pollutants. Being an immobilized material, the $TiO_2$/clay bilayer system also allows the discharge of treated water without filtration and can be continuously reused.

Previously, Nawi et al. (2010, 2011), Nawi and Sabar (2012) had reported on the fabrication of immobilized $TiO_2$–chitosan layered composite on glass plates for the synergistic photocatalytic-adsorptive process in the degradation of anionic reactive red 4 (RR4) dye (Nawi et al. 2011), Nawi and Sabar (2012) and phenol (Jawad and Nawi 2012) from aqueous solution. These studies showed that apart from the simultaneous photocatalytic-adsorptive processes that occurred to remove the pollutants efficiently, the enhanced removal of organic pollutants was also attributed to the change of the optical property of $TiO_2$ upon the addition of chitosan. The photoluminescence spectroscopy analysis done revealed that the integration of chitosan with $TiO_2$ reduced the recombination of the photo-generated electron–hole pairs and prolong the availability of the charge carriers, and hence allowing the photocatalytic efficiency to improve remarkably.

To the best of our knowledge, works involving combination of $TiO_2$ and bentonite in the form of an immobilized bilayer system have not been reported yet in the literature despite bentonite being another popular natural adsorbent. This paper describes the fabrication of the immobilized bentonite composite on a glass plate with high applicability as the adsorbent sub-layer. A glutaraldehyde (GLA)-cross-linked polyvinyl alcohol (PVA) or PVAG was utilized as the adhesive for the immobilization of bentonite on glass plates or BEN–PVAG/GP. Then, a layer of $TiO_2$ was coated on the BEN–PVAG/GP to form a P-25$TiO_2$/BEN–PVAG/GP bilayer system.

Therefore, the objective of this work was to provide an in-depth study of the adsorption characteristics of BEN–PVAG which was used as the sub-layer in the P-25$TiO_2$/BEN–PVAG/GP bilayer system. For this purpose, methylene blue (MB) was chosen as the model pollutant. The second objective was to evaluate the photocatalytic-adsorptive activity and reusability of the fabricated P-25$TiO_2$/BEN–PVAG/GP plate for the removal of MB where the results were compared against the immobilized $TiO_2$ mono layer on a glass plate (P-25$TiO_2$/GP) and suspended $TiO_2$ particles.

## Materials and methods

### Chemicals and reagents

Bentonite (BEN) was purchased from Sigma-Aldrich. Glutaraldehyde (GLA) was a product of Merck. Fumed silica ($SiO_2$) and ammonium persulfate (APS) were bought from Sigma-Aldrich. Concentrated hydrochloric acid (HCl, 12 M), dichloromethane and toluene were procured from QRëC. Sodium hydroxide (NaOH) pellets were purchased from Merck. Potassium nitrate ($KNO_3$) and nitric acid ($HNO_3$) were obtained from BDH Chemicals Ltd. and QRëC. The Degussa P-25 $TiO_2$ nanoparticles (P-25$TiO_2$, 80 % anatase, 20 % rutile) was obtained from Acros Organics, Belgium. The epoxidized natural rubber (ENR-50, 50 % epoxidization) and polyvinyl chloride (PVC) were supplied by Kumpulan Guthrie Sdn. Bhd. and Petrochemicals (M) Sdn. Bhd., respectively. Methylene blue (MB, Colour Index Number: 52015, Chemical formula: $C_{16}H_{18}ClN_3S{\cdot}3H_2O$, molecular weight: 373.90 g $mol^{-1}$, $\lambda_{max}$: 661 nm) was provided by Sigma-Aldrich. The molecular structure of MB is shown in Supplementary Fig. 1. 1000 mg $L^{-1}$ MB stock solution was prepared by dissolving 0.1 g of MB powder with ultra-pure water in 100-mL volumetric flask. The stock solution was then diluted accordingly to obtain the desired concentration.

Polyvinyl alcohol (PVA) powder (88 % hydrolysed, molecular weight: 88, 000 g $mol^{-1}$) was obtained from Acros Organics. The 8 % (w/v) PVA solution was prepared by dissolving 40 g of the PVA powder in 250 mL of ultra-pure water. To prepare the ~10 % (w/v) ENR-50 solution, 24.8 ± 0.05 g of ENR-50 was refluxed in 250 mL of toluene at 88–90 °C until all of the ENR-50 was completely dissolved in the toluene and an adhesive-like and sticky solution was formed.

### Preparation of the immobilized bentonite composite (BEN–PVAG)

To prepare the BEN–PVAG coating formulations, 6 g of BEN was first mixed with 32 mL of 8 % (w/v) PVA solution. Next, 0.20 g of $SiO_2$ was added to the mixture, followed by 10 mL of 0.05 M GLA and 0.56 g of APS in 10 mL of ultra-pure water. Then, 1 mL of 12 M HCl was added to the mixture. Finally, 25 mL of ultra-pure water was then added slowly to dilute the mixture. After that, the colloidal mixture of BEN–PVAG was homogenized by grinding using a ball mill grinder (Pascall Engineering Grinder) for 30 min at 60 rpm. The homogenized BEN–PVAG colloidal solution was then coated onto a glass plate of dimension 45 × 70 × 20 mm by using a nylon brush to produce the immobilized BEN–PVAG composite on a glass plate (BEN–PVAG/GP). The BEN–PVAG/GP was later dried and conditioned at 100 °C for 30 min. The loading of BEN–PVAG on the glass plate can be obtained by subtracting the initial weight of the glass plate from the total weight of the dried BEN–PVAG/GP plate. The BEN/PVA/GLA/$SiO_2$/APS mass ratio in the optimum BEN–PVAG was 120: 51:1:4:11.

### Preparation of immobilized P-25$TiO_2$/GP and P-25$TiO_2$/BEN–PVAG/GP

The immobilized P-25$TiO_2$/GP was prepared according to the simple dip-coating method previously reported by Nawi and Zain (2012). Briefly, 0.80 g of PVC solids was first dissolved in 35 mL of dichloromethane via 1 h of ultra-sonication. After that, 4 g of the 10 % (w/v) ENR-50 solution was added to the dissolved PVC solution before adding 65 mL of toluene and 6 g of P-25$TiO_2$. The optimum mass ratio of P-25$TiO_2$/ENR-50/PVC for the formulation was 7.5: 5: 1. The mixture was then sonicated and homogenized via 8 h of ultra-sonication to form the P-25$TiO_2$ dip-coating formulation. To fabricate the immobilized P-25$TiO_2$/GP, the homogenized P-25$TiO_2$ dip-coating formulation was poured into a coating cell. A cleaned glass plate of dimension 45 × 70 × 20 mm was then dipped up to a depth of 5.5 cm and left for 5 s in the dip-coating formulation before being pulled up manually to deposit the P-25$TiO_2$ composite onto the glass plate. The P-25$TiO_2$-coated glass plate was dried using a hair dryer to vaporize the solvent. One side of the coated glass plate was scraped off and then weighed. The loading of P-25$TiO_2$ composite on the glass plate can be obtained by subtracting the initial weight of the glass plate from the total weight of the dried P-25$TiO_2$/GP plate. The coating–drying–weighing steps were repeatedly carried out until the desired loading was attained. The physical and chemical properties of the immobilized P-25$TiO_2$/GP were well characterized by Nawi and Zain (2012).

For the fabrication of P-25$TiO_2$/BEN–PVAG/GP, a similar dip-coating procedure described above was used. For this purpose, a previously fabricated BEN–PVAG/GP plate was dipped into the P-25$TiO_2$ dip-coating formulation so as to cover up the whole area of the BEN–PVAG and subsequently pulled up manually with a consistent pulling rate between each dipping to obtain a deposition of the photocatalyst. The coated glass plate was dried completely using a hair dryer to vaporize the solvent after which the smooth side of the coated glass plate was scraped off and again carefully weighed. The difference of weight between BEN–PVAG/GP plate and its corresponding P-25$TiO_2$/BEN–PVAG/GP plate would provide the weight of the immobilized P-25$TiO_2$ composite photocatalyst. The coating, drying, and weighing

procedure was carried out until the desired loading of the catalyst was obtained. All of the immobilized P-25$TiO_2$/BEN–PVAG/GP were completely air dried at room temperature and stored in plastic dishes prior to use.

Based on the work of Nawi and Zain (2012), the prepared P-25$TiO_2$/GP and P-25$TiO_2$/BEN–PVAG/GP were then subjected to the photo-etching process before being used in order to make it macroporous and enhance the surface area of the immobilized P-25$TiO_2$ composite. The photo-etching process was carried out by immersing the P-25$TiO_2$/GP and P-25$TiO_2$/BEN–PVAG/GP in ultra-pure water and irradiated for 1 h consecutively until 10 h. The irradiated water was replaced with a fresh batch of ultra-pure water after each successive hour of irradiation. The reactor set-up for the photo-etching process was similar to that used for the experiment under light irradiation ("Photocatalytic and adsorptive removal of MB by P-25$TiO_2$/BEN–PVAG/GP" section).

## Characterizations of composites

The elemental composition of BEN shown in the Supplementary Table 1 was detected using energy dispersive x-ray (EDX, model LEO SUPRA 50 VP Field Emission) analysis. The surface morphology of the composites was analysed using a scanning electron microscope (SEM, Model Leica Cambridge S360). The Brunauer–Emmett–Teller (BET) surface area, total pore volume, and average pore diameter of BEN and BEN–PVAG were determined by nitrogen adsorption and desorption isotherms at 77 K using Micromeritics ASAP 2020 V4.00 surface analyzer. The average particle size, $D_{ps}$, of BEN and BEN–PVAG was estimated by using Eq. (1) (Rouquerol et al. 1999):

$$D_{ps} = \frac{6000}{S_{BET} \times \rho} \quad (1)$$

where $S_{BET}$ is the specific BET surface area and $\rho$ is the bulk density ($\rho$ for BEN and BEN–PVAG are 1.010 and 1.067 g $cm^{-3}$, respectively). The analysis on the functional groups was done using a Fourier transform infrared-attenuated total reflection (FTIR-ATR) spectrophotometer (Perkin-Elmer, model system 1600) in the range from 4000 to 650 $cm^{-1}$ in the transmittance mode.

The point of zero charge ($pH_{pzc}$) of the BEN–PVAG composite was determined by the solid addition method (Balistrieri and Murray 1981). A volume of 50 mL of 0.1 M $KNO_3$ solution was transferred to a series of 100-mL conical flasks. The $pH_i$ values of the solution were adjusted from 2 to 12 by adding either 0.1 M $HNO_3$ or NaOH. Then, 0.1 g of BEN–PVAG was added to each flask. The suspensions were agitated and allowed to equilibrate for 48 h, then filtered, and the final pH of the solution ($pH_f$) was noted. The discrepancy between the initial and final pH values ($\Delta pH = pH_f - pH_i$) was plotted versus the $pH_i$. The value of $pH_{pzc}$ can be obtained from the resulting curve that cuts the $pH_i$ axis of the plot.

The X-ray diffraction (XRD) patterns of the composite samples were acquired on a PANalytical X'Pert PRO MRD PW3040 diffractometer with filtered CuK$\alpha$ radiation at a scanning rate of 0.02°/s in continuous mode. The UV–Vis diffused reflectance spectra (DRS) were obtained via a Lambda 35 Perkin Elmer UV–Vis spectrophotometer from 200 to 800 nm, with a diffuse reflectance accessory using a magnesium oxide disc as the reflectance standard.

## Batch adsorption kinetic studies

Batch adsorption experiments were carried out using the experimental set-up shown in the Supplementary Fig. 2. For the adsorption study, the BEN–PVAG plate was placed upright in a custom-made glass cell with dimension of 50 × 80 × 10 mm that can hold up 25 mL of MB solution. The adsorbate solution was agitated with aeration through a Pasteur pipette with air supplied by an aquarium pump (model NS 7200) at a fixed flow rate of 100 mL $min^{-1}$. The set-up was placed inside a fully covered box in order to prevent any exposure towards light irradiation.

The batch adsorption kinetic studies were conducted using a series of 10–80 mg $L^{-1}$ MB solutions. An optimum amount of 0.15 g BEN–PVAG composite immobilized on a glass plate was used, and the initial pH of the MB solutions was fixed at pH 7. The concentration of the MB solutions at the initial and different interval times was monitored using a direct reading ultraviolet–visible (UV–Vis) spectrophotometer (model DR2000 from HACH) at the wavelength of 661 nm, until it reached the equilibrium state at 60 min contact time. The MB sample was taken at every 5 min interval for measurement. The amount of MB adsorbed, $q_t$ at time $t$, was calculated as Eq. (2):

$$q_t = \frac{(C_o - C_t)}{m} \times V \quad (2)$$

where $C_t$ (mg $L^{-1}$) was the concentration of MB at time $t$.

The batch adsorption kinetic study was also carried out in the suspended mode. For this purpose, the previously immobilized BEN–PVAG composite was scrapped off the glass plate and ground and sieved to obtain ±150-µm-mesh-size particles. Similar adsorption set-up and procedures as described earlier for the immobilized system were followed for this suspended mode study.

## Photocatalytic and adsorptive removal of MB by P-25$TiO_2$/BEN–PVAG/GP

Experimental set-up for the adsorption of MB by P-25$TiO_2$/BEN–PVAG/GP was similar to that of the batch

adsorption study of MB by BEN–PVAG shown in the Supplementary Fig. 2. However, for the photocatalytic-adsorptive removal of MB by P-25$TiO_2$/BEN–PVAG/GP under light irradiation, the box covering the custom-made glass cell was removed, and instead, a 45 W compact visible light fluorescent lamp (Phillips, Model E27, 220–240 V, 50–60 Hz) with a visible light irradiance of 400 W $m^{-2}$ and a UV leakage irradiance of 2.80 W $m^{-2}$ was placed in contact with the outer surface of the custom-made glass cell, directly irradiating the coated glass plate. The amount of visible light and UV leakage irradiance was quantified using a radiometer (Solar light Co. PMA 2100) connected with a UV-A and UV-B broadband detector (PMA 2107). The initial concentrations of MB solution used in this study were 10 and 60 mg $L^{-1}$. For the 60 mg $L^{-1}$ MB solution, the fabricated P-25$TiO_2$/BEN–PVAG/GP bilayer system was first applied in the dark for 30 min, after which the same plate was further used for the removal of MB under light irradiation. For comparison purposes, the P-25$TiO_2$/BEN–PVAG/GP was also separately applied for the removal of MB in the dark and under light irradiation. The pH of the MB solution was fixed at 7 and was agitated with aeration through a Pasteur pipette with air supplied by an aquarium pump at a fixed flow rate of 100 mL $min^{-1}$. The removal of MB from the aqueous solution was monitored using a direct reading spectrophotometer at 661 nm.

### Reusability study of P-25$TiO_2$/BEN–PVAG/GP for photocatalytic-adsorptive removal of MB

The reusability of P-25$TiO_2$/BEN–PVAG/GP for the photocatalytic-adsorptive removal of MB was evaluated using a 10 mg $L^{-1}$ solution of MB. For this purpose, the P-25$TiO_2$/BEN–PVAG/GP was used repeatedly for 10 consecutive cycles, whereby each cycle of application took 60 min. In between each cycle of the applications, the immobilized bilayer composite was regenerated under light irradiation in ultra-pure water for 60 min to remove any MB residuals that remained on the surface of the photocatalyst. This study was carried out using the same experimental set-up described in "Photocatalytic and adsorptive removal of MB by P-25$TiO_2$/BEN–PVAG/GP" section. For comparison purposes, the reusability of P-25$TiO_2$/BEN–PVAG/GP in the adsorptive removal of the MB and the reusability of P-25$TiO_2$/GP in the photocatalytic removal of MB was also carried out.

### Error analyses

Due to the inherent bias resulting from linearization of the adsorption kinetics models, the Chi-square statistical analysis was applied as a criterion for the fitting quality (Auta and Hameed 2012). The Chi-square analysis is the sum of the squares of the differences between the experimental data and the calculated model values, with each squared difference divided by the corresponding calculated model values. The mathematical expression of this analysis is as shown in Eq. (3):

$$\chi^2 = \sum \frac{\left(q_e, \exp - q_{e,calc}\right)^2}{q_{e,calc}} \quad (3)$$

where $q_{e,calc}$ (mg $g^{-1}$) is the adsorption capacity at equilibrium calculated from the model, and $q_{e,exp}$ (mg $g^{-1}$) is the experimental values of the equilibrium adsorption capacity. The degree of $\chi^2$ value depicts the proximity of the calculated and experimental values whereby the smaller value of $\chi^2$ indicates lower discrepancies between the values. This analysis was applied to further identify the suitable reaction model apart from referring to the correlation coefficient, $R^2$, values.

In addition, the validity of the fit of the kinetic model for MB adsorption by BEN–PVAG/GP was also evaluated by the sum of squares error (SSE %) analysis and the SSE was calculated using Eq. (4):

$$\mathrm{SSE} = \sqrt{\frac{\sum\left(q_e, \exp - q_{e,calc}\right)^2}{N}} \quad (4)$$

where $N$ is the number of data points. The lower value of SSE determines the best fit of the adsorption model (Natarajan et al. 2014).

## Results and discussion

### Fabrication of the P25$TiO_2$/BEN–PVAG/GP plate

A new novel approach to combine $TiO_2$ with bentonite is to assemble them in an immobilized bilayer form on a glass plate. The bilayer system comprised of two separate composite systems, in which the bentonite composite is made up the adsorbent sub-layer while the top layer consisted of the $TiO_2$ photocatalyst composite. This integration method is considered advantageous due to several reasons:

1. The $TiO_2$/bentonite bilayer system allows the $TiO_2$ to be directly exposed to light irradiation.
2. The bentonite sub-layer has the potential of improving the optical characteristics of the $TiO_2$ layer as well as improving the separation of the photo-generated charge carriers.
3. The bilayer system allows each of the layers to be modified and controlled independently to acquire the desired degree of photocatalysis and adsorption processes.

4. The $TiO_2$/bentonite bilayer system should be more suitable for the simultaneous photocatalytic-adsorptive removal of intensely coloured pollutant at high concentration under light irradiation where photocatalysis alone may fail under this condition.
5. Being an immobilized material, the $TiO_2$/bentonite bilayer system allows the direct discharge of the treated water without filtration and can be continuously reused.

The schematic diagram and cross-sectional micrograph (under x1 K magnification) of the bilayer assembly of P-25$TiO_2$/BEN–PVAG/GP plate are shown in Fig. 1. The fabricated bilayer system was made up of the immobilized BEN–PVAG sub-layer on a glass plate and a P-25$TiO_2$ top layer. The aim was to produce a synergistic photocatalytic-adsorption bilayer system for the enhanced removal of MB. The immobilization of BEN on a glass plate was carried out by using the glutaraldehyde (GLA) cross-linked polyvinyl alcohol (PVAG) as the adhesive. The cross-linking of the PVA adhesive was a necessity in order to overcome its swelling behaviour and to increase its stability so that it can be applied in aqueous media. The cross-linking reaction of PVA with GLA resulted in the formation of acetal groups and ether linkages which decreased the swelling behaviour of the PVA (Mansur et al. 2008). Meanwhile, $SiO_2$ was added to the BEN–PVAG composite as a filler to increase its mechanical resistance (Peng et al. 2006) and APS was applied as an oxidant to initiate the polymerization of hydrogen on the PVA chain (Li et al. 2015). Meanwhile, the P-25$TiO_2$ composite top layer was prepared exactly according to the procedures reported by Nawi and Zain (2012). In brief, the P-25$TiO_2$ composite top layer contained ENR-50 as an emulsifier to homogenize the P-25$TiO_2$ dip-coating formulation. ENR-50 also served as macro-pores precursor since it was susceptible to fast degradation under light irradiation. Therefore, the photocatalytic degradation of ENR-50 during the photo-etching process created pores and consequently enhanced the surface area of the P-25$TiO_2$ composite (Nawi and Zain 2012). On the other hand, the PVC in the composite was found to be photo-resistance, and thus, functioned as adhesive to bind the P-25$TiO_2$ nanoparticles onto the glass plate (Nawi and Zain 2012).

With this arrangement, dual processes involving photocatalysis and adsorption would run simultaneously once the P-25$TiO_2$/BEN–PVAG/GP plate was irradiated with a light source while an experiment run in the dark would yield only the adsorption process. In order to pursue the understanding of the role of BEN–PVAG composite sub-layer in the photocatalytic-adsorptive removal of MB by the P-25$TiO_2$/BEN–PVAG/GP bilayer system, a thorough characterization of the BEN–PVAG composite sub-layer was carried out including its adsorption characteristics.

## Characterization of the BEN–PVAG composite sub-layer and P-25$TiO_2$/BEN–PVAG/GP

The SEM micrographs of BEN and BEN–PVAG composite (x 10 K) are provided in Fig. 2. BEN possessed the typical irregular sheet-like structures which appeared to be very fluffy (Fig. 2a). However, after the inclusion of PVAG to form BEN–PVAG (Fig. 2b), the sheet-like structures were seen foliated where multiple BEN sheets were bound together by PVAG binder to form stacks of thick rigid plates. In addition, all BEN–PVAG surfaces were clearly covered with the PVAG binder which resulted in the formation of rougher surfaces than the original BEN sheets.

The nitrogen adsorption and desorption isotherms of BEN and BEN–PVAG composite at 77 K are given in the Supplementary Fig. 3. According to the IUPAC

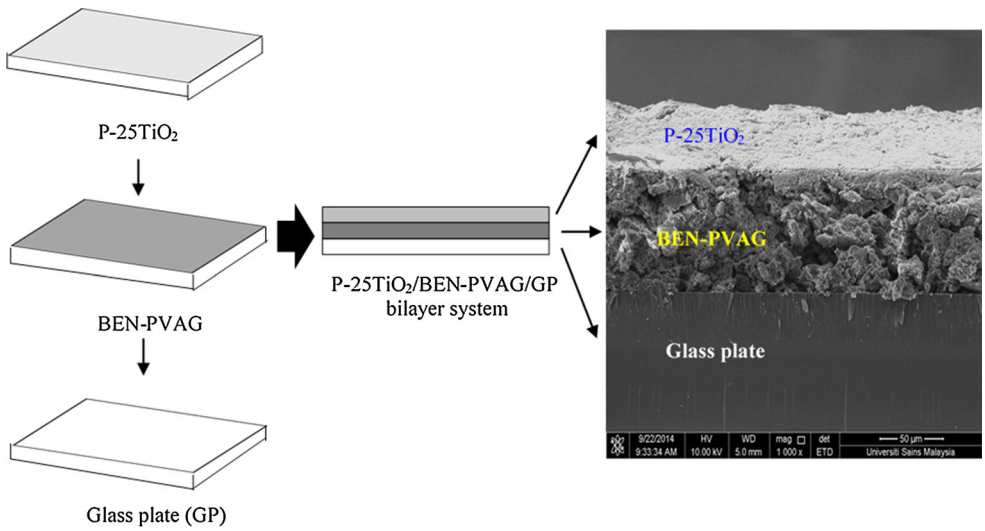


**Fig. 1** Schematic diagram and cross-sectional micrograph (under x1 K magnification) of the assembly of P-25$TiO_2$/BEN–PVAG/GP bilayer system

classification, both BEN and BEN–PVAG composite demonstrated type IV adsorption isotherms with type 4 hysteresis loops, indicative of the existence of the mesoporous structures. The broad hysteresis loop of H4 type indicates the formation of slit-like pores associated with the capillary condensation in mesoporous behaviour (Chiang et al. 2001; Thommes 2010). Clearly, addition of PVAG sharply decreased the adsorption isotherm which indicated a significant decrease in its BET surface area.

The comparisons of the surface and porosity characteristics between BEN and BEN–PVAG are summarized in the Supplementary Table 2. The addition of PVAG to BEN decreased not only the specific surface area, but also the total pore volume and average pore diameter of BEN and expectedly caused an increase in the particle size of BEN–PVAG composite. The average pore diameters of the samples were within the range of 2–10 nm, further confirming that the samples were typical mesoporous materials. These results suggested that the added PVAG was mainly dispersed on the external surfaces of BEN particles (Fig. 2b) where the PVAG molecules could be intercalated into the layers of BEN. Even though PVAG caused a reduction in the BET surface area of the clay, it was an effective adhesive for the immobilization of BEN onto the glass plates. When a BEN–PVAG/GP plate was sonicated for 30 s using ultrasonic with sonic power of 180 W, only 1.4 % BEN–PVAG/GP weight loss was detected.

The FTIR-ATR spectra of (a) BEN and (b) BEN–PVAG are shown in Fig. 3. In the spectra of BEN (Fig. 3a), the band at 3627 $cm^{-1}$ is assigned to the O–H stretching vibration of the Si–OH groups while the band at 3445 $cm^{-1}$ corresponds to the O–H stretching of the adsorbed water molecules in the interlayer and intra-layer (Madejová 2003). The strong band at 1039 $cm^{-1}$ is attributed to the asymmetric stretching mode of Si–OH (Zaitan et al. 2008). The band at 1638 $cm^{-1}$ is assigned to the bending of H–OH bond of water molecules (Madejová 2003). The (Al, Mg)–OH vibration mode is indicated by the band at 525 $cm^{-1}$ (Yang et al. 2010), and the band at 468 $cm^{-1}$ indicates the bending of Si–O–Si bonds (Saleh 2015). After the incorporation of PVAG binder to BEN, the band assigned to the structural –OH of BEN at 3627 $cm^{-1}$ disappeared in the spectra of BEN–PVAG (Fig. 3b). The intensities of the bands ascribed to Si–OH, –OH vibration modes, and Si–O bending of BEN at 1039, 525, and 468 $cm^{-1}$ (Saleh 2015), respectively, were observed to decrease with the introduction of PVAG. In addition, the band belonging to O–H stretching at 3445 $cm^{-1}$ was red-shifted. These changes suggest possible occurrence of hydrogen bonding between the –OH groups of PVAG and Si–O groups of BEN by direct hydrogen bonds or/and hydrogen bridging through $H_2O$ (Kaczmarek and Podgórski 2007). The emergence of band at 1401 $cm^{-1}$ in the

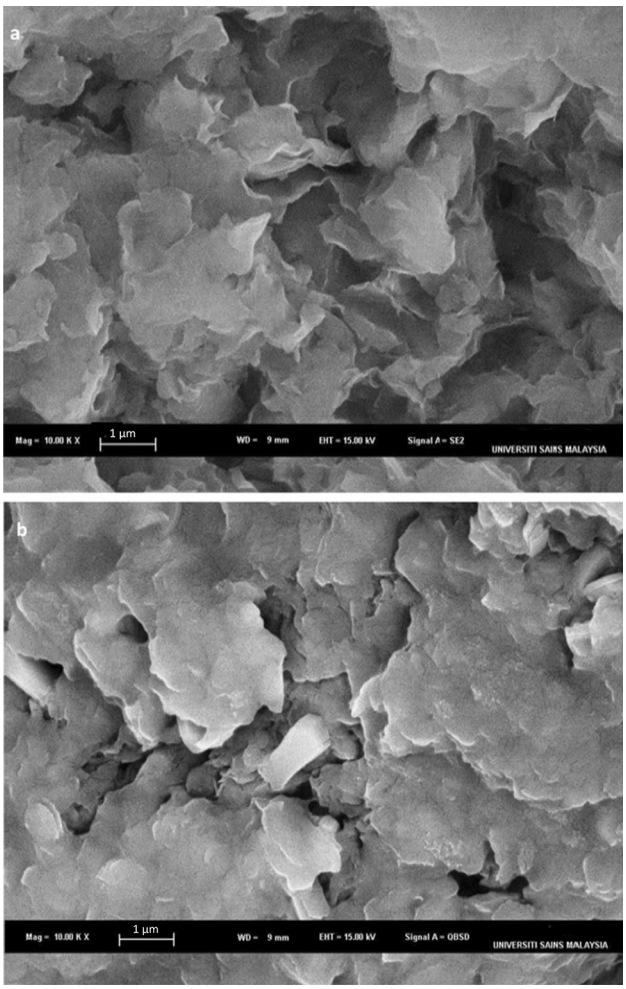


**Fig. 2** SEM images of **a** BEN and **b** BEN–PVAG composite under 10 K times of magnification

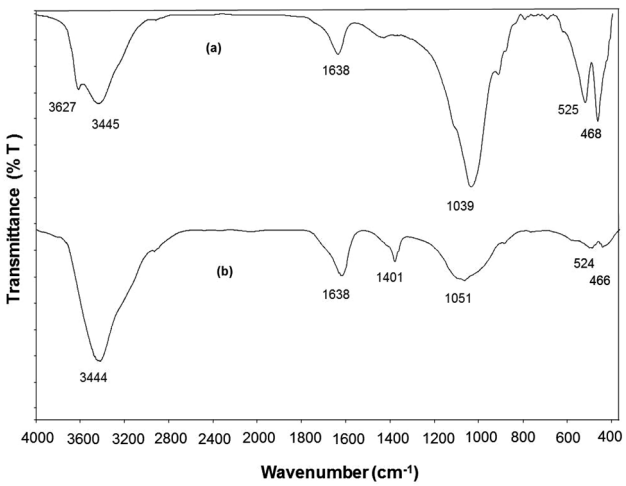


**Fig. 3** FTIR spectrum of (*a*) BEN and (*b*) BEN–PVAG

spectra of BEN–PVAG (Fig. 3b) is attributed to the deformation vibrations of $CH/CH_2$ groups of PVAG (Mansur et al. 2008).

The $pH_{pzc}$ of an adsorbent determines whether the surface of the adsorbent is positively or negatively charged as a function of pH and hence significantly affects the uptake of the absorbate at different solution pH. The plot of ΔpH versus $pH_i$ for BEN and BEN–PVAG (Supplementary Fig. 4) shows that the $pH_{pzc}$ of BEN and BEN–PVAG was pH 7.6 and 3.0, respectively. This lower $pH_{pzc}$ value for BEN–PVAG was the result of the presence of PVA. Similar observation was reported by Moayedi et al. (2011) where adding PVA to both peat and kaolinite caused a significant reduction in isoelectric point (IEP) of soil samples. This implied that at pH >3, the surface of the BEN–PVAG is negatively charged, while for BEN, the negative surface was achieved when the pH was >7.6. As the pH of the solution was increased beyond 3.0, BEN–PVAG surface should become increasingly more favourable for the adsorption of the cationic MB dye. Therefore, in terms of coulombic attraction, adding PVAG to BEN had expanded the working pH range for the adsorption of cationic MB dye by the adsorbent into the acidic condition.

The XRD patterns for BEN, BEN–PVAG, P-25$TiO_2$, and the optimum P-25$TiO_2$/BEN–PVAG/GP are illustrated in Supplementary Fig. 5. The (001), (003), (020–110), (130–200), and (060–033) diffraction peaks of the montmorillonite component of the bentonite powder are observed at $2\theta = 5.80°$, 17.87°, 19.89°, 34.92°, and 62.51° with distances of 15.23, 4.97, 4.46, 2.57, and 1.49 Å, respectively (Caglar et al. 2009). Meanwhile, the diffraction peaks attributed to the non-clay components, quartz, and dolomite, occur at $2\theta = 26.73°$ and 29.28° with (101) and (104) distances of 26.73 and 29.28 Å, respectively. As seen in the XRD pattern of BEN–PVAG, the diffraction peak of BEN at $2\theta = 62.51°$ diminished on the addition PVAG, implying partial destruction of the crystallinity of BEN by the PVAG binder. The change in the BEN structure may have arisen from the use of concentrated HCl in the preparation of PVAG binder which could drastically affect the octahedral and tetrahedral sites of the clay (Bhattacharyya and Gupta 2008). The (001) peak of BEN–PVAG was shifted to a low angle ($2\theta = 4.83$) as compared to that of bentonite powder at $2\theta = 5.80$, indicating an increase in the basal spacing between ordered layers of bentonite from 15.23 to 18.30 Å. The expansion in the basal spacing of BEN–PVAG suggested that there was intercalation of the PVAG binder within the interlayer space of the bentonite (İşci et al. 2004).

The XRD characteristics of P-25$TiO_2$/BEN–PVAG/GP were found to be identical to that of the pristine P-25$TiO_2$, but there was reduction in the intensities of the peaks. This shows that the presence of BEN–PVAG as the adsorbent sub-layer for P-25$TiO_2$ in the fabrication of P-25$TiO_2$/BEN–PVAG/GP lowered the crystallinity of the photocatalyst, potentially due to the presence of the polymeric binders. The XRD pattern of P-25$TiO_2$/BEN–PVAG/GP shows diffraction peaks at $2\theta = 25.3°$, 37.8°, 48.0°, 53.9°, 55.1°, 62.6°, 66.3°, and 68.9° which correspond to the (101), (103), (200), (105), (211), (213), (116), and (220) crystalline plane of the anatase phase, respectively (Gnanasekaran et al. 2015). Other peaks at $2\theta = 27.5°$ and 41.4° are attributed to the (110) and (111) diffraction planes of rutile. The new diffraction peaks observed at $2\theta = 26.59°$ and 34.72° indicated the presence of bentonite (quartz (101) and montmorillonite (130–200)) within the P-25$TiO_2$/BEN–PVAG/GP bilayer system.

The UV–Vis DRS of BEN–PVAG/GP, P-25$TiO_2$/GP, and P-25$TiO_2$/BEN–PVAG/GP in absorbance mode is presented in Supplementary Fig. 6(a). For the entire region from 250 to 800 nm, the DRS of BEN–PVAG/GP did not exhibit adsorption edge and showed high absorbance in the visible light region. It can be observed that the P-25$TiO_2$/BEN–PVAG/GP demonstrated better absorbance of light with wavelength between 400 and 800 nm than the P-25$TiO_2$/GP, and a slight red shift of the main adsorption edge was also noticed. These changes affected the effective band gap energy of the photocatalyst. Thus, the obtained UV–Vis DRS was used to estimate the band gap energy (eV) using the Kulbeka–Munk (K–M) function and Tauc plot. The K–M function, $F_{K-M}$ used is shown in Eq. (5):

$$F_{K-M} = \frac{(1 - R^2)}{2R} \tag{5}$$

where $R$ is the reflectance and the indirect band gap factors $(F_{K-M} \times E)^{1/2}$ used for Tauc plots are constructed against photon energy ($E$) for determination of the band gap energy (Tauc et al. 1966). The Tauc plots for P-25$TiO_2$/GP and P-25$TiO_2$/MT-PVA/GP are presented in the Supplementary Fig. 6(b), in which their band gap energy values estimated from the intercept of the tangents to the plots were 3.04 and 2.98, respectively. The band gap energy of P-25$TiO_2$/BEN–PVAG/GP was slightly smaller than that of P-25$TiO_2$/GP indicating that lower photon energy was needed to photo-activate P-25$TiO_2$/BEN–PVAG/GP as compared to P-25$TiO_2$/GP. This attribute may be due to the formation of sub-states by metal ions of bentonite and oxygen defects within the valence and conduction band of P-25$TiO_2$. Thus, the electrons are not directly excited to the conduction band since these unoccupied sites can capture the photo-excited electrons. Similar observation had been seen by Tahir and Amin (2013) and Todorova et al. (2014) for their prepared $TiO_2$–clay composite.

## Adsorption characteristics of BEN–PVAG composite

The adsorption kinetics of 10–80 mg $L^{-1}$ of MB onto the immobilized BEN–PVAG was evaluated for 60 min contact time and the results are shown in Fig. 4. The adsorption of MB at all concentrations occurred rapidly at the initial stage, followed by a slower phase before reaching the equilibrium state. The adsorption was fast for the first 10 min, which suggests rapid external diffusion and surface adsorption (Nawi et al. 2010). This was basically due to the abundance of active sites available at preliminary stage of adsorption. With further increase in time, the adsorption started slowing down gradually before reaching the equilibrium state. Longer time was needed to reach equilibrium at higher concentrations, as there was a tendency for the adsorbate to penetrate deeper within the interior surface of the immobilized BEN–PVAG layer and utilized more active sites. The contact time needed to reach equilibrium conditions increased from 25 to 55 min as the concentration of MB increased from 10 to 80 mg $L^{-1}$. The diffusion of dye molecules towards the deeper sub-layer of BEN–PVAG was expected to be a relatively slow process. Similar observation was noted by Nawi et al. (2010) and Benhouria et al. (2015) who investigated the adsorption of reactive red 4 onto immobilized chitosan and uptake of methylene blue by calcium alginate–bentonite-activated carbon composite, respectively.

The two main types of adsorption kinetics models, namely the reaction-based models and the diffusion-based models, were then applied to fit the obtained adsorption batch equilibrium data at different concentrations. The

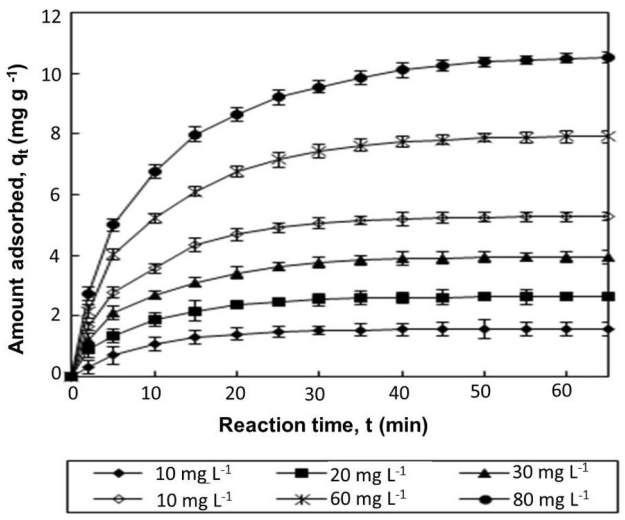


**Fig. 4** Effect of contact time on the adsorption of MB onto BEN–PVAG/GP at different concentrations

reaction-based kinetic models were used to find out the adsorption rate and to explain the sorbate–sorbent interaction that occurred during the adsorption process. Meanwhile, the diffusion-based kinetic models were employed to elucidate a series of diffusion mechanism steps that affected the adsorption process rate.

### *Reaction-based models*

In the reaction-based models, the kinetics of MB adsorption onto the immobilized BEN–PVAG was evaluated using the linear forms of pseudo-first-order (Ho and McKay 1998), pseudo-second-order (Ho and McKay 2003) and Elovich (Chien and Clayton 1980) models as shown in Eq. (6), (7) and (8), respectively:

$$\mathrm{Log}(q_e - q_t) = \mathrm{Log}\, q_e - \frac{k_1}{2.303} t \tag{6}$$

$$\frac{t}{q_t} = \frac{1}{k_2 q_e^2} + \frac{t}{q_e} \tag{7}$$

$$q_t = \frac{1}{\beta} \ln(\alpha\beta) + \frac{1}{\beta} \ln t \tag{8}$$

where $q_t$ and $q_e$ (mg $g^{-1}$) are the amount of MB adsorbed onto BEN–PVAG at contact time, $t$, and at equilibrium, $k_1$, $k_2$ and α are the adsorption rate constants of pseudo-first-order, pseudo-second-order, and Elovich models, respectively, while β (g $mg^{-1}$) corresponds to the extent of surface coverage and activation energy for chemisorption. The pseudo-first-order, pseudo-second-order and Elovich plots for the adsorption process are provided in the Supplementary Fig. 7. The values of $k_1$ and $q_e$ for the pseudo-first-order model were determined from the slopes and intercepts of the plot of Log ($q_e - q_t$) versus t. The calculated values of $k_2$ and $q_e$ for the pseudo-second order model can be obtained from the intercept and slope of $\frac{t}{q_t}$ versus $t$. As for the Elovich model, the calculated values of α and β are obtained from the plot of $q_t$ against ln t. Their respective calculated kinetic parameter values are presented in Table 1, whereby it is shown that slightly higher correlation coefficient, $R^2$, was obtained for the pseudo-second-order model as compared with the pseudo-first-order model. As the differences between the $R^2$ values for both pseudo-first and pseudo-second order models were very low at all concentrations, Chi squared analysis was employed to further determine the best fit of the adsorption kinetic model (Auta and Hameed 2012). The smaller $\chi^2$ values obtained from the Chi square analysis further affirmed that the adsorption of MB onto BEN–PVAG was better explained by the pseudo-second order kinetic model. This conclusion was further supported by the calculated $q_{e,cal}$ value obtained from pseudo-first-order kinetic model

**Table 1** Kinetic parameters of pseudo-first-order, pseudo-second-order, Elovich, intra-particle diffusion and Boyd models at different concentrations of MB

| Model | Parameters | MB concentration (mg $L^{-1}$) | | | | | |
|---|---|---|---|---|---|---|---|
| | | 10 | 20 | 30 | 40 | 60 | 80 |
| Pseudo-first order | $q_{e,exp}$ (mg $g^{-1}$) | 1.711 | 2.735 | 4.157 | 5.481 | 8.420 | 10.935 |
| | $q_{e,calc}$ (mg $g^{-1}$) | 1.685 | 2.515 | 3.730 | 4.770 | 8.239 | 10.280 |
| | $R^2$ | 0.989 | 0.986 | 0.987 | 0.988 | 0.988 | 0.988 |
| | $k_1$ ($min^{-1}$) | 0.117 | 0.113 | 0.106 | 0.104 | 0.102 | 0.086 |
| | $\chi^2$ | 0.0004 | 0.0177 | 0.0439 | 0.0922 | 0.0039 | 0.0392 |
| | SSE (%) | | | 4.5 | | | |
| Pseudo-second order | $q_{e,calc}$ (mg $g^{-1}$) | 1.730 | 2.807 | 4.234 | 5.643 | 8.547 | 11.364 |
| | $R^2$ | 0.998 | 0.996 | 0.995 | 0.996 | 0.994 | 0.993 |
| | $k_2$ (g $mg^{-1}$ $min^{-1}$) | 0.112 | 0.100 | 0.058 | 0.046 | 0.025 | 0.017 |
| | $X^2$ | 0.0002 | 0.0019 | 0.0014 | 0.0049 | 0.0019 | 0.0017 |
| | SSE (%) | | | 2.0 | | | |
| Elovich | $\beta$ (g $mg^{-1}$) | 2.627 | 1.854 | 1.210 | 0.906 | 0.575 | 0.426 |
| | $\alpha$ (mg $g^{-1}$ $min^{-1}$) | 0.558 | 1.635 | 0.848 | 2.984 | 3.559 | 4.184 |
| | $R^2$ | 0.946 | 0.961 | 0.976 | 0.965 | 0.980 | 0.990 |
| Intra-particle diffusion (immobilized) | $k_{id1}$ | 0.368 | 0.490 | 0.700 | 0.992 | 1.467 | 1.916 |
| | $R^2$ | 0.979 | 0.991 | 0.978 | 0.986 | 0.978 | 0.979 |
| Intra-particle diffusion (suspended) | $k_{id1}$ | 3.581 | – | – | 8.390 | – | 19.330 |
| | C | 0.592 | – | – | 8.708 | – | 16.028 |
| | $R^2$ | 0.999 | – | – | 0.997 | – | 0.998 |
| Boyd (immobilized) | $R^2$ | 0.998 | 0.999 | 0.997 | 0.998 | 0.997 | 0.987 |
| Boyd (suspended) | $R^2$ | 0.862 | – | – | 0.852 | – | 0.899 |

which showed higher sum of square error (SSE %) than that of the value determined from the pseudo-second-order kinetic model. This implied that the adsorption rate determining step of MB onto the immobilized BEN–PVAG composite was governed by chemical processes that involved the formation of complexes or electron exchange between the adsorbate molecules and the adsorbent. Other workers who studied the adsorption of MB by clay materials also observed similar phenomenon (Cottet et al. 2014). The adsorption rate constant of pseudo-second order $k_2$, declined as the initial concentrations of MB increased, showing that the amount of time required to reach equilibrium became longer with increased initial concentrations of MB.

The chemical adsorption kinetics of MB onto BEN–PVAG was further verified by applying the Elovich model which described the occurrence of chemisorption processes on adsorbents with heterogeneous surface. By referring to their $R^2$ values in Table 1, it can be deduced that the Elovich model can also be used to explain the adsorption kinetics of MB onto BEN–PVAG. Thus, it can be assumed that during the adsorption process, the initial uptake of MB onto immobilized BEN–PVAG was rapid, but later slowed down as a function of time due to the coverage of adsorption sites as well as interaction between MB and BEN–PVAG composite. In addition, the heterogeneity of BEN–PVAG surface was further affirmed by the adsorption isotherm study which showed that the obtained adsorption data fitted well with the Freundlich isotherm model (see Supplementary Table 3). The Freundlich isotherm model (Freundlich 1906) is usually employed to explain the adsorption process that occurs on heterogeneous surfaces with contacts between the adsorbed molecules. The adsorption of MB by the suspended BEN particles on the other hand obeyed Langmuir isotherm model indicating that it was a monolayer adsorption process which occurred on a uniform surface with finite number of adsorption sites and there were no interactions among the adsorbed molecules on the surface (Cottet et al. 2014).

Supplementary Table 4 provides a comparison of maximum adsorption capacity ($q_{max}$) for various types of clay-based adsorbent for the uptake of MB. The adsorption capacity of MB onto the suspended BEN–PVAG was quite comparable to most of the listed adsorbents. However, there was a significant reduction in the adsorption capacity for BEN–PVAG/GP due to the effect of immobilization which reduced its BET surface area. Despite so, BEN–

PVAG/GP still possessed better adsorption capacity than some of the clay-based adsorbents such as natural palygorskite, Al pillared clay, pyrophyllite, and pickled-ground pyrophyllite. Therefore, it was proven that the prepared immobilized BEN–PVAG/GP was suitable to be used as the adsorbent sub-layer in the fabrication of the P-25$TiO_2$/BEN–PVAG/GP bilayer system.

*Diffusion-based models*

In bulk system adsorption, the diffusion mechanism of sorbate onto and within the sorbent particles directly affects the adsorption rate. Essentially, there are four steps that occur in the adsorption process: (1) Transport of sorbate from the bulk of the solution to the exterior film surrounding of the adsorbent (liquid phase mass transfer). (2) Movement of sorbate across the external liquid film boundary layer to external surface sites (film diffusion). (3) Migration of sorbate within the pores of the sorbent by the intra-particle diffusion. (4) Sorption of sorbate at internal surface sites (internal mass transfer).

Due to the turbulent condition of the aerated solution, the transport of sorbate from the bulk of the solution to the exterior film surrounding the adsorbent (step 1) can be neglected. Step 4 can also be neglected, due to the rapid nature of the sorption process at the surface sites. Therefore, the two main mechanisms may involve step 2 and step 3. In order to assess this, the Weber–Morris plot (Weber and Morris 1963) of $q_t$ versus $t^{1/2}$ was evaluated. If the rate-limiting step is due to the intra-particle diffusion, a plot of $q_t$ against $t^{1/2}$ should yield a straight line passing through the origin (Poots et al. 1976). The commonly used intra-particle diffusion equation is expressed as Eq. (9):

$$q_t = k_{id} t^{1/2} + C \tag{9}$$

where $k_{id}$ is the intra-particle diffusion rate constant (mg $g^{-1}$ $min^{-1/2}$) and the intercept C is proportional to the degree of the boundary layer thickness. As seen in Fig. 5a, the Weber-Morris plots for all solution concentrations involving the immobilized BEN–PVAG are linear and pass through the origin in the first phase of the adsorption process, in particular from 0 to 30 min. According to Weber-Morris, good linearization of data is expected for the initial stage of the adsorption process if the rate-controlling factor is intra-particle diffusion. The intra-particle diffusion kinetic model parameters are given in Table 1. Good correlation coefficient, $R^2$, values were obtained for the first stage of the adsorption when the linear line of $q_t$ against $t^{1/2}$ plots were forced through the origin. The result indicates that the effect of the external film control is minimal and almost negligible in this adsorption system. Therefore, it could be concluded that the intra-particle diffusion was the predominant mechanism throughout the

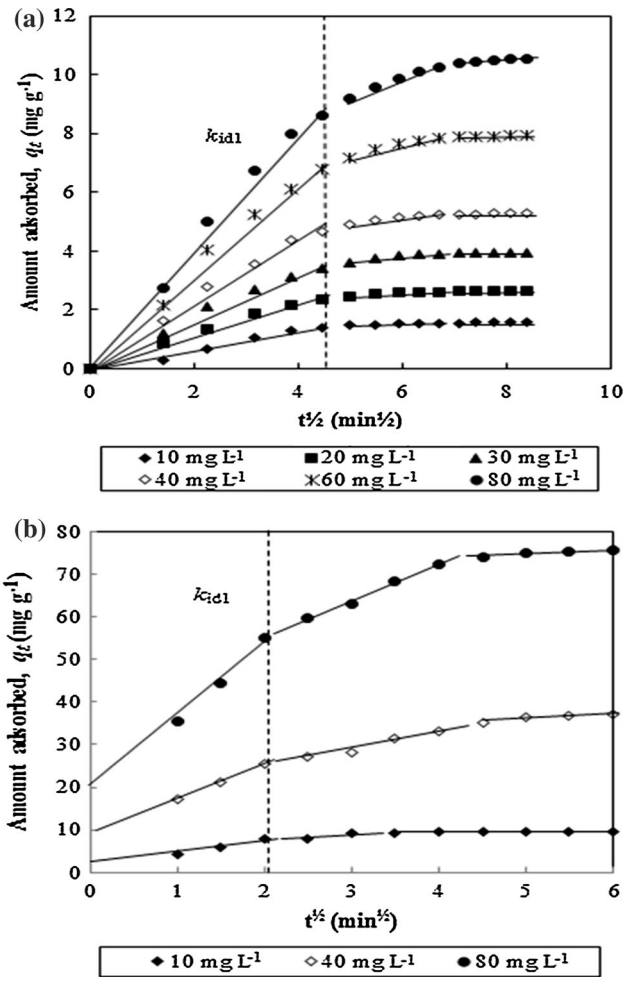


**Fig. 5** Intra-particle diffusion kinetic plot for adsorption of MB onto **a** immobilized and **b** suspended BEN–PVAG at different concentrations

bulk of the sorption process. The initial linear portion can be considered as the fast adsorption process of MB by the mesoporous structures of the system. When the sorption of the mesoporous structure reached saturation, the MB molecules diffused in the microporous internal surface pores within the particle and then were sorbed by the internal surface of the particles. Apparently, as the MB molecules diffused in the micropores of the particle, the diffusion resistance increased, which caused the diffusion rate to decrease (stage 2). When the MB concentration in the solution was decreased, the diffusion rate became lower and the diffusion processes reached the final equilibrium stage (stage 3).

The intra-particle plot in Fig. 5b shows that the diffusion of MB onto the suspended BEN–PVAG also occurred in three stages for all tested concentrations although at 10 mg $L^{-1}$, the adsorption process reached equilibrium state in a shorter period of time as compared to the rest of the concentrations. Longer time was required to attain equilibrium

at higher concentrations as more active sites were needed to accommodate more MB molecules. The first linear portion corresponded to the external mass transfer. The second linear portion represented the intra-particle diffusion, and the third linear portion indicated the adsorption/desorption equilibrium. Interestingly, unlike the MB adsorption process by the immobilized BEN–PVAG, none of the linear portions in Fig. 5b passed through the origin, implying that the intra-particle diffusion was not the sole or the main rate-controlling step in the MB adsorption process by the suspended system. The intercept of the plot deviated from the point of origin, implying that an external mass transfer influenced the process greatly due to their significant intercept values of the plots. The intercept C values of the plots which represent the extent of the boundary layer thickness increased proportionally with the increasing MB concentration, suggesting that the boundary layer effect was greater at higher concentration. The characteristic of this plot has been widely obtained for the adsorption of textile dyes onto suspended clay particles as observed by other workers (Elass et al. 2011; Gil et al. 2011).

In brief, this finding indicated that once the system was immobilized on a flat surface support material such as glass plates, the rate-controlling step became dominated with intra-particle diffusion. This was probable since the effectiveness of the adsorption process would depend on the mobility or diffusion of the MB molecules from the outer surface of the immobilized clay particles through stacks of the inner immobilized clay particles until no more diffusion occurred due to the low concentration of the solution.

The different MB diffusion mechanism exhibited by the immobilized and suspended BEN–PVAG was further confirmed by applying the Boyd kinetic equation (Boyd et al. 1947) shown in Eq. (10):

$$F = 1 - \frac{6}{\pi^2}\sum_{n=1}^{\infty}\frac{1}{n^2}\exp(-n^2\mathrm{Bt}) \tag{10}$$

where $F$ represents the fraction of sorbate adsorbed at reaction time, t, calculated from the following Eq. (11):

$$F = \frac{q_t}{q_e} \tag{11}$$

By transforming Eq. (10), the approximate values of Bt can be obtained from Eq. (12) and (13), as suggested by Reichenberg (1953):

$$F \text{ values} < 0.85, \mathrm{Bt} = \left(\pi 1/2 - \left(\pi - \frac{\pi^2 F}{3}\right)^{1/2}\right)2 \tag{12}$$

$$F \text{ values} > 0.85, \mathrm{Bt} = -0.4977 - \ln(1 - F) \tag{13}$$

The value of Bt can be calculated according to each of the $F$ values and the resulting Bt values are plotted against t. If the Boyd plot yields a straight line which passes through the origin, this indicates that the adsorption process is governed by the intra-particle diffusion mechanism as it is the slowest stage in the process; otherwise, the adsorption process is controlled by film diffusion. The yielded Boyd plots for the immobilized and suspended BEN–PVAG are illustrated in the Supplementary Fig. 8(a) and (b), respectively, and their correlation coefficient, $R^2$ values are presented in Table 1. The Boyd plot obtained for the immobilized BEN–PVAG was linear and passed through the origin, whereas the plot for the suspended BEN–PVAG was neither linear nor passed through the origin, suggesting that when the adsorbent composite was immobilized on a flat solid support, the rate of uptake of MB was intra-particle diffusion controlled while in the suspended system, film diffusion mechanism governed the adsorption process. Evidently, this result correlated positively with the finding presented by the Weber-Morris intra-particle diffusion model discussed earlier.

*MB adsorption mechanism by BEN–PVAG/GP*

Based on the surface property and adsorption behaviour of BEN–PVAG/GP and MB molecules, a plausible adsorption mechanism for MB adsorption onto the immobilized BEN–PVAG/GP was suggested as shown in Fig. 6. As illustrated in Fig. 6a, the surface of BEN–PVAG/GP was negatively charged due to the presence of hydroxyl groups from PVA and silicate groups from BEN which provided adsorption sites for the coulombic interactions with the cationic MB molecules. On the other hand, the immobilized form of BEN–PVAG dictated two important factors governing the extent of adsorption, namely the loading which translated itself into the thickness of the immobilized adsorbent layer and the mass transport of the pollutant via intra-particle diffusion. Therefore, Fig. 6b depicts the diffusion of MB from the external surface of BEN–PVAG/GP towards its interior particles. In order to simplify the discussion on the mechanism of MB adsorption onto the immobilized BEN–PVAG/GP, Fig. 6b is illustrated without the presence of PVAG. As the MB adsorption process by the immobilized BEN–PVAG was governed by intra-particle diffusion, the effectiveness of the system relies on the mobility of MB within the immobilized bentonite particles until no more diffusion could happen due to either extremely low concentration of adsorbate or all adsorption sites had been occupied. Thus, at low concentration, i.e. 10 mg $L^{-1}$, only adsorption sites at a shallow depth of the BEN–PVAG were taken up and caused the inner immobilized bentonite composite to be excessive. However, at higher concentration, i.e. 60 mg $L^{-1}$, the MB diffused deeper into the interior of the immobilized bentonite until the adsorption

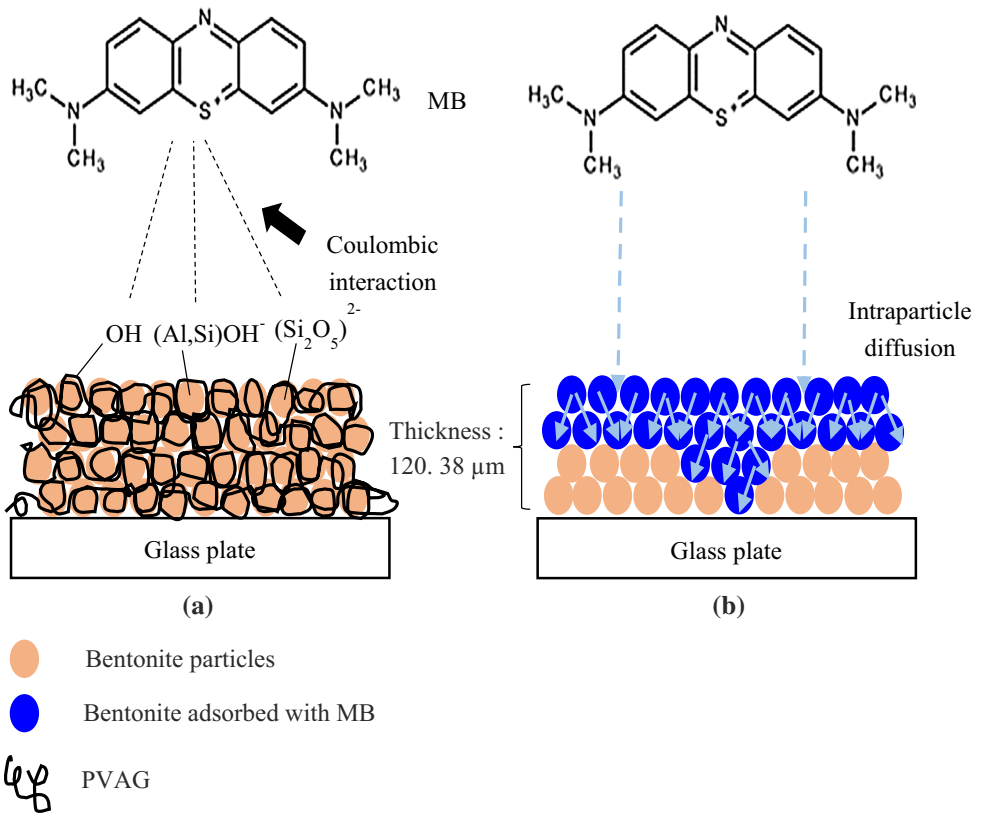


**Fig. 6** Schematic illustration of the **a** interactions and **b** adsorption diffusion process between MB and BEN–PVAG/GP

equilibrium was reached. In terms of equilibrium time, the more dilute MB solution utilized thinner depth of the immobilized adsorbent layer resulting in a faster equilibrium but smaller adsorption capacity due to the large excessive adsorption sites. However, the process of the intra-particle diffusion would take longer time for the higher concentration samples since it diffused deeper resulting in the longer equilibrium time and higher adsorption capacity.

## Synergistic photocatalytic-adsorptive performance of the immobilized P-25TiO$_2$/BEN–PVAG bilayer system

The fabrication of P-25TiO$_2$/BEN–PVAG bilayer system was optimized by using BEN–PVAG composite with different BEN/ PVAG weight/weight ratio using a fixed loading of 4.91 mg cm$^{-2}$ of the adsorbent composite as the sub-layer and the fixed loading of P-25TiO$_2$ at 1.33 mg cm$^{-2}$ as the top layer (Nawi and Zain 2012). The optimization was done by comparing their resulted apparent rate constant, $k_{app}$ which can be calculated from the Langmuir–Hinshelwood (L–H) kinetic model. The L–H kinetic model is widely applied to describe the kinetics of photocatalytic removal of organic pollutants in aqueous solution (Gupta et al. 2012). The L–H kinetic equation shown in Eq. (14):

$$\ln \frac{C_o}{C_t} = k_{app} t \tag{14}$$

where $C_o$ (mg L$^{-1}$) and $C_t$ (mg L$^{-1}$) are the concentration of MB at 0 and $t$ min, respectively. The apparent rate constant, $k_{app}$ (min$^{-1}$), can be obtained from the slope of the $\ln \frac{C_o}{C_t}$ versus $t$ plot. As shown in the Supplementary Fig. 9, the optimum ratio of BEN/PVAG for the BEN–PVAG composite was at 2:1.

Supplementary Fig. 10 (a) compares the adsorption of MB by the immobilized BEN–PVAG/GP plate and the P-25TiO$_2$/BEN–PVAG/GP plate under dark condition. It is observed that the deposition of P-25TiO$_2$ on top of the BEN–PVAG/GP did not inhibit the diffusion of MB towards the adsorbent sub-layer. However, apparently the P-25TiO$_2$/BEN–PVAG/GP bilayer system required a longer time to reach adsorption equilibrium state even though the final adsorption capacity for both BEN–PVAG/GP plate and the P-25TiO$_2$/BEN–PVAG/GP plate was similar. The increase in equilibrium time for the adsorption process of MB by the bilayer system was due to the increase in mass transfer resistance of MB molecules towards the BEN–PVAG sub-layer due to the presence of

P-25 $TiO_2$ top layer which had acted as a porous barrier layer. Most important, Supplementary Fig. 10(a) proved that the adsorption process of MB by the BEN–PVAG adsorbent sub-layer functioned well despite the presence of the P25$TiO_2$ top layer.

The synergistic effect of the fabricated P-25$TiO_2$/BEN–PVAG/GP bilayer system was preliminarily assessed by comparing the photocatalytic and adsorption performance of the bilayer P-25$TiO_2$/BEN–PVAG/GP against the immobilized monolayer P-25$TiO_2$/GP for the removal of 10 and 60 mg $L^{-1}$ MB. Photolysis of MB was carried out as the control test. The percentage of the remaining of MB via photolysis, photocatalysis, and adsorption was calculated using the following Eq. (15):

$$\text{MB removal}\,(\%) = \frac{(C_o - C_t)}{C_o} \times 100 \qquad (15)$$

where $C_o$ and $C_t$ are the initial concentration and at time $t$, respectively.

The result of this evaluation is illustrated in the Supplementary Fig. 10(b). Photolysis and adsorption by P-25$TiO_2$ did not cause any removal of MB. However, under the photocatalytic process, the P-25$TiO_2$ managed to remove 73.6 % of MB in 60 min. Meanwhile, P-25$TiO_2$/BEN–PVAG/GP system was an excellent adsorbent for MB where 90 % of MB was removed within 60 min which was essentially due to the presence of BEN–PVAG sub-layer. Subsequently, when P-25$TiO_2$/BEN–PVAG was employed for the photocatalytic-adsorptive removal of MB, it was found that 99.6 % of the MB was removed. Despite portraying similar removal efficiency, the removal rate of MB by P-25$TiO_2$/BEN–PVAG/GP under photocatalytic-adsorptive process was notably higher than the adsorption process, implying that the synergistic adsorption-photocatalysis had definitely occurred. This observation clearly revealed that during the removal of MB by P-25$TiO_2$/BEN–PVAG/GP under light irradiation, both adsorption and photocatalytic processes occurred simultaneously whereby the photocatalytic process was provided by the P-25$TiO_2$ top layer while the adsorption process was contributed by the BEN–PVAG/GP adsorbent sub-layer. As evidently shown earlier in the Supplementary Fig. 10 (a), the MB molecules were well adsorbed by the P-25$TiO_2$/BEN–PVAG/GP bilayer system due to the accessible porous P-25$TiO_2$ top layer. Thus, under light irradiation, removal of MB by photocatalytic reactions occurred in addition to the adsorption process. In order to further illustrate the concurrent occurrences of adsorption and photocatalytic processes by P-25$TiO_2$/BEN–PVAG/GP under light irradiation, experiments involving 60 mg $L^{-1}$ MB were carried out in the dark and under light irradiation. The results are presented in Fig. 7a. In this case, removal of MB was first carried out in the dark for 30 min (curve I) thus ensuring that only adsorption process occurred. Then, the light was switched on for the rest of the experiment where under this condition, both photocatalysis and adsorption processes contributed towards the removal of MB (curve II). During the experiment in the dark, the rate of removal of MB via the adsorption process was calculated to be 0.0239 $min^{-1}$. However, when the P-25$TiO_2$/BEN–PVAG/GP bilayer system was exposed to light irradiation, the rate of removal of MB jumped to 0.0528 $min^{-1}$ indicating that both photocatalytic and adsorption processes manifested simultaneously. Evidently, the MB adsorption process happened at a slower rate in comparison with the combined MB adsorption and photocatalytic processes. This phenomenon was further illustrated by subjecting the bilayer system separately for the MB removal in the dark and under light irradiation. The MB removal rate in the dark and under light irradiation was 0.0240 and 0.0483 $min^{-1}$, respectively. Once again, the MB removal rate under the concurrent photocatalytic-adsorption processes was two times higher than that of the adsorption process, indicating that two processes happening at the same time. For comparison purposes, the removal of MB was also carried out under light irradiation using P-25$TiO_2$/GP monolayer system in which it was revealed that the photocatalytic removal of MB occurred minimally at a removal rate of 0.0029 $min^{-1}$. This result can be attributed to the reduction in photon energy reaching the surface of P-25$TiO_2$/GP as the light irradiation intensity was obstructed by the intense colour of the 60 mg $L^{-1}$ MB solution. Thus, the photoactivation of P-25$TiO_2$/GP was hampered and this reduced the photocatalytic performance. Moreover, at high concentration, notable amount of light irradiation may be absorbed by the MB rather than P-25$TiO_2$/GP and this may also cause reduction in the photocatalytic efficiency. This is in line with the works by Gupta et al. (2012) and Sobana et al. (2015) who witnessed similar phenomenon during the photocatalytic removal of dyes at high concentration. Subsequently, this highlights the significant applicability of the P-25$TiO_2$/BEN–PVAG/GP bilayer composite system for the removal of highly coloured textile dyes effluents whereby first, the MB molecules were removed through adsorption by the BEN–PVAG/GP sub-layer adsorbent via the porous P-25$TiO_2$ top layer and then the MB concentrated within the interface of the P-25$TiO_2$ and BEN–PVAG was removed by photocatalytic process. This is plausible because the adsorption of MB by the BEN–PVAG/GP adsorbent sub-layer reduced the MB concentration of the solution which also reduced the colour intensity of the MB solution. This would permit better penetration of light energy towards the surface of P-25$TiO_2$ so that more oxidizing radicals can be

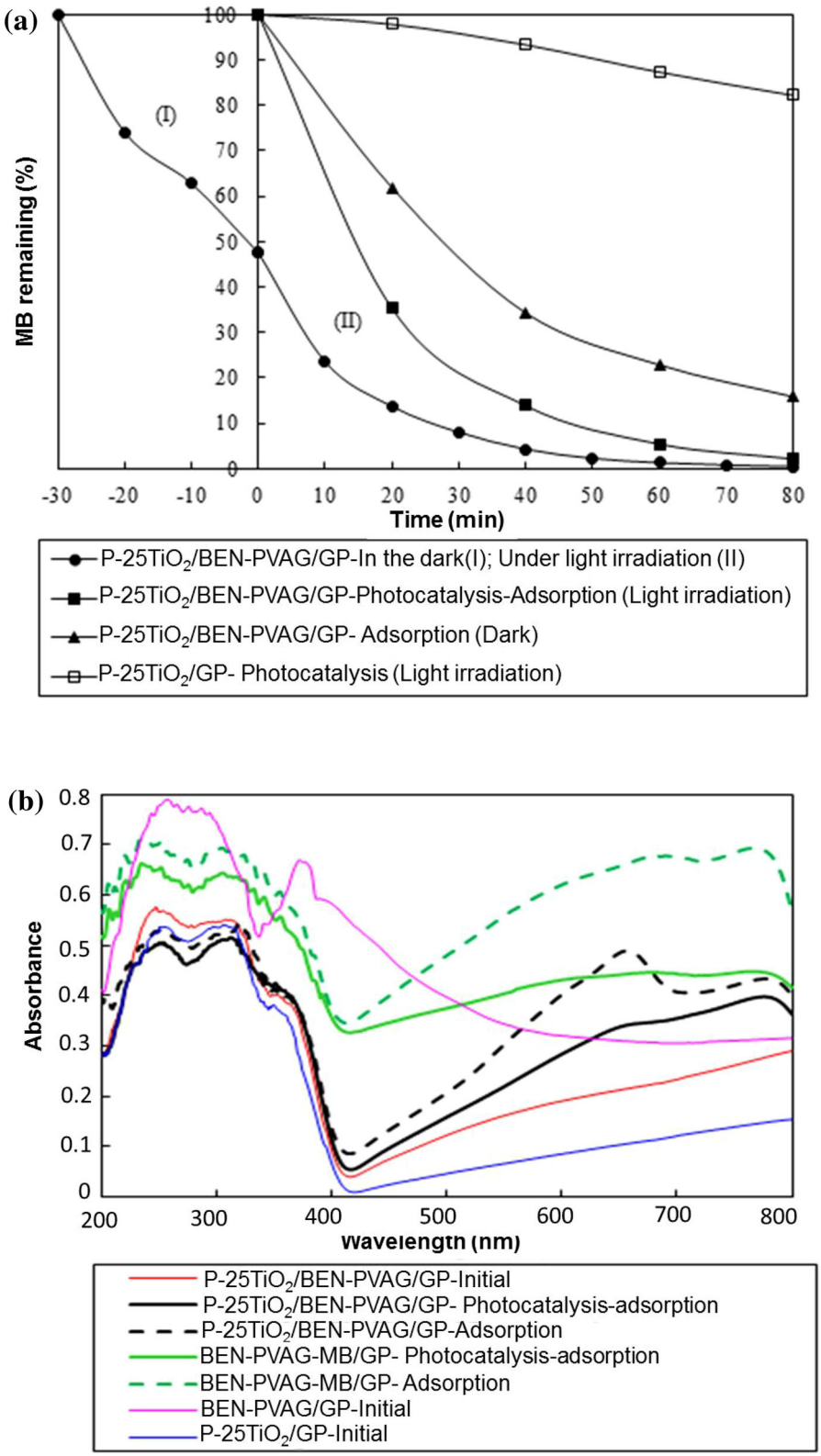


**Fig. 7** **a** Photocatalytic and adsorptive removal of 60 mg $L^{-1}$ MB by P-25$TiO_2$/BEN–PVAG/GP and **b** UV–Vis DR spectra of the applied P-25$TiO_2$/BEN–PVAG/GP

generated and diffused from the surface of P-25$TiO_2$ to the interface of P-25$TiO_2$/BEN–PVAG to photocatalytically remove the adsorbed MB molecules.

This phenomenon was further investigated by carrying out the diffused reflectance spectroscopic analysis of the surface of the composites after they had been used in the

**Table 2** Summary of the photocatalytic-adsorptive removal of MB by various $TiO_2$–clay composite

| Catalyst | Duration (min) | [MB] (mg $L^{-1}$) | Degradation (%) | Light source | References |
|---|---|---|---|---|---|
| $TiO_2$–aluminium pillared montmorillonite | 120 | 16 | 80 | 10 W UVB lamp | Fatimah et al. (2010) |
| $TiO_2$ pillared montmorillonite | 60 | 30 | 99 | 250 W high pressure Hg lamp | Chen et al. (2013) |
| $TiO_2$/natural Portuguese clay | 1200 | 10 | 96.5 | 9 W germicidal lamp | Hajjaji et al. (2013) |
| TiZnAl-LDH | 250 | 35 | 100 | 125 W high pressure Hg lamp | Sahu et al. (2013) |
| ZnAlTi-LDH | 120 | 10 | 100 | Solar light (7.6 × 104 lx) | Wang et al. (2014) |
| HT-DS/$TiO_2$/Fe | 120 | 24 | 100 | 125 W Hg vapour lamp | Miranda et al. (2015) |
| 20 %$TiO_2$/zeolite 4A | 100 | 10 | 100 | 125 W Hg vapour lamp | Nagarjuna et al. (2015) |
| $TiO_2$@ZnFe-LDH clay | 150 | 32 | 98 | 100 W Hg lamp | Seftel et al. (2015) |
| P-25$TiO_2$/BEN–PVAG/GP | 45 | 10 | 100 | 45 W fluorescent lamp | This work |
| P-25$TiO_2$/BEN–PVAG/GP | 80 | 60 | 100 | 45 W fluorescent lamp | This work |

removal of MB either in the dark or light irradiation. The DRS spectra in Fig. 7b show that during the adsorption process only (in the dark), the MB molecules were evidently deposited on the P-25$TiO_2$ top layer of the P-25$TiO_2$/BEN–PVAG/GP bilayer composite, as indicated by the intense peak at 661 nm. In comparison, the intensity of this peak for the P-25$TiO_2$/BEN–PVAG/GP reacted with MB under light irradiation was clearly lower, indicating that the MB molecules that were deposited on the P-25$TiO_2$ top layer had been photocatalytically degraded. Upon the removal of the P-25$TiO_2$ top layer from the P-25$TiO_2$/BEN–PVAG/GP bilayer system, the observed broad peak ranging from 500 to 800 nm for the BEN–PVAG/GP sub-layer from the bilayer system that was used in the dark (the adsorption process only) was far more intense than that of the one applied under light irradiation for the photocatalysis-adsorption process. This outcome revealed that during the adsorption process only (in the dark condition) by the bilayer composite, almost all of the removed MB molecules ended up deposited on the BEN–PVAG/GP adsorbent sub-layer. On the other hand, when the system was applied under light irradiation, the broad peak ranging from 500 to 800 nm of the BEN–PVAG/GP DRS spectrum significantly decreased in intensity. This could only mean that less MB ended up in the adsorbent sub-layer since a large fraction of the MB molecules was photocatalytically degraded leaving only smaller fraction for adsorption by the adsorbent sub-layer.

Table 2 summarizes the applications of various $TiO_2$–clay composites in the literatures for the photocatalytic-adsorptive removal of MB. The results prove that the P-25$TiO_2$/BEN–PVAG/GP prepared in this work offers highly effective and time-saving solution to degrade MB under low energy light source, even at concentration as high as 60 mg $L^{-1}$. By using the immobilized P-25$TiO_2$/BEN–PVAG/GP bilayer system, filtration of the treated MB solution is redundant, and being an immobilized material, the P-25$TiO_2$/BEN–PVAG/GP can be continuously reused. Moreover, the immobilized bilayer system can be assimilated into a flow-through reactor for convenient photocatalytic-induced water treatment purposes.

The P-25$TiO_2$/GP and P-25$TiO_2$/BEN–PVAG/GP were repeatedly used for 10 cycles of reuse for the photocatalytic-adsorption removal of MB in order to compare their reusability. Figure 8a depicts the degradation of MB based on the percentage remaining efficiency plots, while Fig. 8b illustrates their apparent rate constants throughout the 10 cycles of reuse. The P-25$TiO_2$/BEN–PVAG/GP exhibited better removal of MB as compared to P-25$TiO_2$/GP throughout the 10 cycles of reuse, whereby an average of $99.67 \pm 0.14$ % and $70.08 \pm 3.72$ % of MB removal were achieved by P-25$TiO_2$/BEN–PVAG/GP and P-25$TiO_2$/GP, respectively. Meanwhile, the average apparent rate constants for the removal of MB by the immobilized bilayer P-25$TiO_2$/BEN–PVAG/GP and monolayer P-25$TiO_2$/GP were $0.096 \pm 0.006$ and $0.021 \pm 0.002$ $min^{-1}$, respectively. The apparent rate constant for the removal of MB by the immobilized bilayer P-25$TiO_2$/BEN–PVAG/GP was on the average 4.6 folds higher than the monolayer P-25$TiO_2$/GP throughout the ten cycles of reuse. Additionally, although the photocatalytic superiority of various types of clay combined with $TiO_2$ in the degradation of MB had been reported (Chen et al. 2013; Hajjaji et al. 2013), the immobilization of clay-$TiO_2$ via the layer by layer assembly onto a glass plate as carried out in our present work permitted excellent reusability but also sustainable rate of MB removal throughout the entire ten cycles of reuse. On top of that, the treated water could be discharged directly without the need for the costly and cumbersome filtration of the catalyst particles as normally required using the conventional suspended approach.

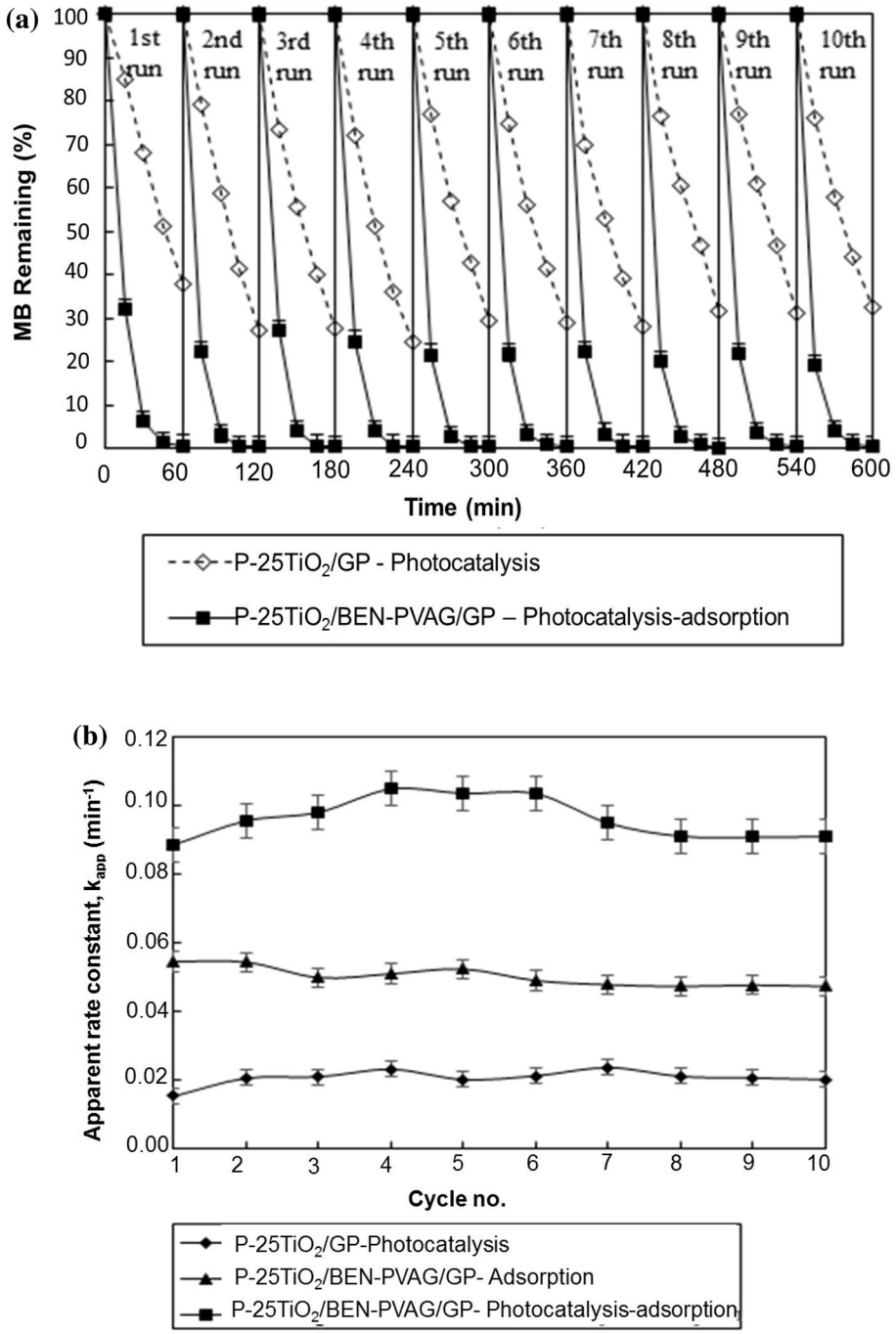


**Fig. 8** **a** Photocatalytic efficiencies of P-25$TiO_2$/GP and P-25$TiO_2$/BEN–PVAG/GP during 10 repeated cycles of MB degradation and **b** their corresponding apparent rate constants

## Conclusion

The fabricated BEN–PVAG/GP plate possessed a good adsorption affinity towards MB in an aqueous solution and was then applied as the adsorbent sub-layer for the fabrication of the synergistic photocatalysis-adsorption of the bilayer P-25$TiO_2$/BEN–PVAG/GP system. Analysis of the adsorption data depicted that the rate of adsorption conformed to the pseudo-second-order model. This work also proved that the application of BEN–PVAG in different

modes, immobilized or suspended, had great impact on the diffusion mechanism of the adsorption process. When the system was immobilized on a flat surface support material such as glass plates, the rate-controlling step became dominated with intra-particle diffusion while in the suspended system, film diffusion mechanism governed the adsorption process. The preliminary photocatalytic evaluation results showed that the P-25$TiO_2$/BEN–PVAG/GP plate exhibited higher MB removal rate by 4.6 and 5.3 times as compared with the monolayer P-25$TiO_2$/GP plate and suspended P-25$TiO_2$, respectively. This proved the importance of incorporating BEN–PVAG into the P-25$TiO_2$/BEN–PVAG/GP system for the enhanced rate of removal MB from aqueous solution via the simultaneous occurrence of the dual photocatalysis-adsorption processes. Most importantly, P-25$TiO_2$/BEN–PVAG/GP plate exhibited excellent reusability with sustainable rate of removal throughout the entire ten cycles of reuse.

**Acknowledgments** The authors are thankful to Universiti Sains Malaysia for funding this research through the Postgraduate Research Grant Scheme (USM-RU-PGRS: 1001/PKIMIA/844101). We would also like to thank Malaysia's Ministry of Higher Learning for the scholarship given under the MyBrain15 program.

## References

Akar ST, Uysal R (2010) Untreated clay with high adsorption capacity for effective removal of C. I. Acid Red 88 from aqueous solutions: batch and dynamic flow mode studies. Chem Eng J 162:591–598

Ararem A, Bouras O, Arbaoui F (2011) Adsorption of caesium from aqueous solution on binary mixture of iron pillared layered montmorillonite and goethite. Chem Eng J 172:230–236

Auta M, Hameed BH (2012) Modified mesoporous clay adsorbent for adsorption isotherm and kinetics of methylene blue. Chem Eng J 198–199:219–227

Balistrieri LS, Murray JW (1981) The surface chemistry of goethite (α-FeOOH) in major ion seawater. Am J Sci 281:788–806

Benhouria A, Islam MA, Zaghouane-Boudial H, Boutahala M, Hameed BH (2015) Calcium alginate-bentonite-activated carbon composite beads as highly effective adsorbent for methylene blue. Chem Eng J 270:621–630

Bhattacharyya KG, Gupta SS (2008) Influence of acid activation on adsorption of Ni(II) and Cu(II) on kaolinite and montmorillonite: kinetic and thermodynamic study. Chem Eng J 136:1–13

Bovey J, Kooli F, Jones W (2006) Preparation and characterization of Ti-pillared acid-activated clay catalysts. Clay Miner 31:501–506

Boyd GE, Adamson AW, Myers LS (1947) The exchange adsorption of ions from aqueous solutions by organic zeolites. II. Kinetics. J Am Chem Soc 69:2836–2848

Caglar B, Afsin B, Tabak A, Eren E (2009) Characterization of the cation-exchanged bentonites by XRPD, ATR, DTA/TG analyses and BET measurement. Chem Eng J 149:242–248

Chen H, Zhao J, Zhong A, Jin Y (2011) Removal capacity and adsorption mechanism of heat-treated palygorskite clay for methylene blue. Chem Eng J 174:143–150

Chen D, Du G, Zhu Q, Zhou F (2013) Synthesis and characterization of $TiO_2$ pillared montmorillonites: application for methylene blue degradation. J Colloid Interf Sci 409:151–157

Chiang YC, Chiang PC, Huang CP (2001) Effects of pore structure and temperature on VOC adsorption on activated carbon. Carbon 39:523–534

Chien SH, Clayton WR (1980) Application of Elovich equation to the kinetics of phosphate release and sorption in soils. Soil Sci Soc Am J 44:265–268

Cottet L, Almeida CAP, Naidek N, Viante MF, Lopes MC, Debacher NA (2014) Adsorption characteristics of montmorillonite clay modified with iron oxide with respect to methylene blue in aqueous media. Appl Clay Sci 95:25–31

Damardji B, Khalaf H, Duclaux L, David B (2009) Preparation of $TiO_2$-pillared montmorillonite as photocatalyst Part I. Microwave calcinations, characterisation and adsorption of a textile azo dye. Appl Clay Sci 44:201–205

Elass K, Laachach A, Alaoui A, Azzi M (2011) Removal of methyl violet from aqueous solution using a stevensite-rich clay from Morocco. Appl Clay Sci 54:90–96

Eren E (2009) Investigation of a basic dye removal from aqueous solution onto chemically modified Unye bentonite. J Hazard Mater 166:88–93

Faisal M, Tariq MA, Muneer M (2007) Photocatalysed degradation of two selected dyes in UV-irradiated aqueous suspensions of titania. Dyes Pigments 72:233–239

Fatimah I, Wang S, Narsito Wijaya K (2010) Composites of $TiO_2$–aluminum montmorillonite: synthesis, characterization and photocatalytic degradation of methylene blue. Appl Clay Sci 50:588–593

Freundlich HMF (1906) Über die adsorption in lösungen. Z Phys Chem 57:385–470

Gil A, Assis FCC, Albeniz S, Korili SA (2011) Removal of dyes from wastewaters by adsorption on pillared clays. Chem Eng J 168:1032–1040

Gnanasekaran L, Hemamalini R, Ravichandran K (2015) Synthesis and characterization of $TiO_2$ quantum dots for photocatalytic application. J Saudi Chem Soc 19:589–594

Gupta VK, Saleh TA (2013) Sorption of pollutants by porous carbon, carbon nanotubes and fullerene—an overview. Environ Sci Pollut Res 20:2828–2843

Gupta VK, Jain R, Mittal A, Saleh TA, Nayak A, Agarwal S, Sikarwar S (2012) Photo-catalytic degradation of toxic dye amaranth on $TiO_2$/UV in aqueous suspensions. Mater Sci Eng C 32:12–17

Gupta VK, Kumar R, Nayak A, Saleh TA, Barakat MA (2013) Adsorptive removal of dyes from aqueous solution onto carbon nanotubes: a review. Adv Colloid Interface Sci 193–194:24–34

Hajjaji W, Ganiyu SO, Tobaldi DM, Andrejkovicova S, Pullar RC, Rocha F, Labrincha JA (2013) Natural Portuguese clayey materials and derived $TiO_2$-containing composites used for decolouring methylene blue (MB) and orange II (OII) solutions. Appl Clay Sci 83–84:91–98

Ho YS, McKay G (1998) Comparison of chemisorptions kinetic models applied to pollutant removal on various sorbents. Trans Inst Chem Eng 76B:332–336

Ho YS, McKay G (2003) Sorption of dyes and copper ions into biosorbents. Process Biochem 38:1047–1061

İşci S, Günister E, Ece ÖI, Güngör N (2004) The modification of rheologic properties of clays with PVA effect. Mater Lett 58:1975–1978

Jamil TS, Ghaly MY, Fathy NA, Abd el-halim TA, Österlund L (2012) Enhancement of $TiO_2$ behavior on photocatalytic oxidation of MO dye using $TiO_2$/AC under visible irradiation and sunlight radiation. Sep Purif Technol 98:270–279

Jawad AH, Nawi MA (2012) Oxidation of crosslinked chitosan–epichlorohydrine film and its application with $TiO_2$ for phenol removal. Carbohydr Polym 90:87–94

Kaczmarek H, Podgórski A (2007) The effect of UV-irradiation on poly(vinyl alcohol) composites with montmorillonite. J Photochem Photobiol A 191:209–215

Li J, Zhang L, Gu J, Sun Y, Ji X (2015) Cross-linking of poly (vinyl alcohol) with N, N′-methylene bisacrylamide via a radical reaction to prepare pervaporation membranes. RSC Adv 5:19859–19864

López MJ, Guisado G, Vargas-García MG, Suárez-Estrella F, Moreno J (2006) Decolorization of industrial dyes by ligninolytic microorganisms isolated from composting environment. Enzyme Microb Tech 40:42–45

Madejová J (2003) FTIR techniques in clay mineral studies. Vib Spectrosc 31:1–10

Mansur HS, Sadahira CM, Souza AN, Mansur AAP (2008) FTIR spectroscopy characterization of poly (vinyl alcohol) hydrogel with different hydrolysis degree and chemically crosslinked with glutaraldehyde. Mater Sci Eng C 28:539–548

Miranda LDL, Bellato CR, Milagres JL, Moura LG, Mounteer AH, de Almeida MF (2015) Hydrotalcite-$TiO_2$ iron oxide intercalated with the anionic surfactant dodecylsulfate in the photocatalytic degradation of methylene blue dye. J Environ Manage 156:225–235

Moayedi H, Asadi A, Moayedi F, Huat BBK (2011) Zeta potential of tropical soil in presence of polyvinyl alcohol. Int J Electrochem Sci 6:1294–1306

Nagarjuna R, Roy S, Ganesan R (2015) Polymerizable sol-gel precursor mediated synthesis of $TiO_2$ supported zeolite-4A and its photodegradation of methylene blue. Micropor Mesopor Mater 211:1–8

Natarajan TS, Bajaj HC, Tayade RJ (2014) Preferential adsorption behaviour of methylene blue dye onto surface hydroxyl group enriched $TiO_2$ nanotube and its photocatalytic regeneration. J Colloid Interface Sci 433:104–114

Nawi MA, Sabar S (2012) Photocatalytic decolourisation of Reactive Red 4 dye by an immobilised $TiO_2$/chitosan layer by layer system. J Colloid Interface Sci 372:80–87

Nawi MA, Zain SM (2012) Enhancing the surface properties of the immobilized Degussa P-25 $TiO_2$ for the efficient photocatalytic removal of methylene blue from aqueous solution. Appl Surf Sci 258:6148–6157

Nawi MA, Sabar S, Jawad AH, Ngah WW (2010) Adsorption of reactive red 4 by immobilized chitosan on glass plates: towards the design of immobilized $TiO_2$–chitosan synergistic photocatalyst-adsorption bilayer system. Biochem Eng J 49:317–325

Nawi MA, Jawad AH, Sabar S, Wan Ngah WS (2011) Immobilized bilayer $TiO_2$/chitosan system for the removal of phenol under irradiation by a 45 watt compact fluorescent lamp. Desalination 280:288–296

Peng Z, Kong KX, Li SD, Spiridonov P (2006) Polyvinyl alcohol/silica nanocomposite: its morphology and thermal degradation kinetics. J Nanosci Nanotechnol 6:3934–3938

Poots VJP, McKay G, Healy JJ (1976) The removal of acid dye from effluent using natural adsorbents—II Wood. Water Res 10:1067–1070

Radeka M, Markov S, Lončar E, Rudić O, Vučetić S, Ranogajec J (2014) Photocatalytic effects of $TiO_2$ mesoporous coating immobilized on clay roofing tiles. J Eur Ceram Soc 34:127–136

Reichenberg D (1953) Properties of ion exchange resins in relation to their structure. Part III. Kinetics of exchange. J Am Chem Soc 75:589–598

Rossetto E, Petkowicz DI, Santos JHZ, Pergher SBC, Penha FG (2010) Bentonites impregnated with $TiO_2$ for photodegradation of methylene blue. Appl Clay Sci 48:602–606

Rouquerol F, Rouquerol J, Sing K (1999) Adsorption by powders and porous solids. Academic Press, London

Sahu RK, Mohanta BS, Das NN (2013) Synthesis, characterization and photocatalytic activity of mixed oxides derived from ZnAlTi ternary layered double hydroxides. J Phys Chem Solids 74:1263–1270

Saleh TA (2015) Isotherm, kinetic, and thermodynamic studies on Hg(II) adsorption from aqueous solution by silica-multiwall carbon nanotubes. Sci Pollut Res, Environ. doi:10.1007/s11356-015-4866-z

Saravanan R, Karthikeyan S, Gupta VK, Sekaran G, Narayanan V, Stephen A (2013) Enhanced photocatalytic activity of ZnO/CuO nanocomposite for the degradation of textile dye on visible light illumination. Mater Sci Eng C 33:91–98

Seftel EM, Niarchos M, Mitropoulos Ch, Mertens M, Vansant EF, Cool P (2015) Photocatalytic removal of phenol and methylene-blue in aqueous media using $TiO_2$@LDH clay nanocomposites. Catal Today 252:120–127

Selvakumar KV, Basha CA, Prabhu HJ, Kalaichelvi P, Nelliyan S (2010) The potential of free cells of *Pseudomonas aeruginosa* on textile dye degradation. Bioresour Technol 101:2678–2684

Silva MMF, Oliveira MM, Avelino MC, Fonseca MG, Almeida RKS, Filho ECS (2012) Adsorption of an industrial anionic dye by modified-KSF-montmorillonite: evaluation of the kinetic, thermodynamic and equilibrium data. Chem Eng J 203:259–268

Sobana N, Subash B, Swaminathan M (2015) Effect of operational parameters on photodegradation of Direct Blue 53 by silver loaded-titania under ultraviolet and solar illumination. Mater Sci Semicond Proc 36:149–155

Tahir M, Amin NS (2013) Photocatalytic reduction of carbon dioxide with water vapors over montmorillonite modified $TiO_2$ nanocomposites. Appl Catal B Environ 142–143:512–522

Tauc J, Grigorovici R, Vancu A (1966) Optical properties and electronic structure of amorphous germanium. Phys Status Solidi B 15:627–637

Thommes M (2010) Physical adsorption characterization of nanoporous materials. Chem Ing Tech 82:1059–1073

Todorova N, Giannakopoulou T, Karapati S, Petridis D, Vaimakis T, Trapalis C (2014) Composite $TiO_2$/clays materials for photocatalytic NOx oxidation. Appl Surf Sci 319:113–120

Wang W, Zheng B, Deng Z, Feng Z, Fu L (2013) Kinetics and equilibriums for adsorption of poly (vinyl alcohol) from aqueous solution onto natural bentonite. Chem Eng J 214:343–354

Wang X, Wu P, Huang Z, Zhu N, Wu J, Li P, Dang Z (2014) Solar photocatalytic degradation of methylene blue by mixed metal oxide catalysts derived from ZnAlTi layered double hydroxides. Appl Clay Sci 95:95–103

Weber WJ, Morris JC (1963) Kinetics of adsorption on carbon from solution. J Sanit Eng Div Am Soc Civ Eng 89:31–59

Weng CH, Pan YF (2007) Adsorption of a cationic dye (methylene blue) onto spent activated clay. J Hazard Mater 144:355–362

Yang S, Zhao D, Zhang H, Lu S, Chen L, Yu X (2010) Impact of environmental conditions on the sorption behaviour of Pb(II) in Na–bentonite suspensions. J Hazard Mater 183:632–640

Zaitan H, Bianchi D, Achak O, Chafik T (2008) A comparative study of the adsorption and desorption of *o*-xylene onto bentonite clay and alumina. J Hazard Mater 153:852–859

Zhang J, Zhou Y, Jiang M, Li J, Sheng J (2015) Removal of methylene blue from aqueous solution by adsorption on pyrophyllite. J Mol Liq 209:267–271

Zhu HY, Othman JA (2002) Novel composites of $TiO_2$ (anatase) and silicate nanoparticles. Chem Mater 14:5037–5044